Dynamic Mode Decomposition for Shape Estimation of a Large Flexible Spacecraft

Curtis A. Merrill* and Derek A. Paley†
University of Maryland, College Park, Maryland, 20742

Recent advancements in space technology have increased the demand for larger spacecraft, which are prone to structural oscillations that can complicate attitude control and degrade performance. Mitigating these oscillations requires sophisticated control laws and state estimation methods that are difficult to perform in real-time with limited computation power. This paper proposes a flexible spacecraft model consisting of a hub and flexible appendage. The flexible appendage is modeled via discretization into flexibly connected rigid elements. To facilitate computational feasibility of real time estimation, dynamic mode decomposition (DMD) applied to numerical simulation data of the system yields a reduced-order linear model. A Kalman filter estimates the DMD mode amplitudes of the system from a limited set of measurements which, using the DMD modes, are used to estimate the full state of the spacecraft. Numerical simulations demonstrate that this framework yields accurate state estimates for significantly reduced computational cost.

Nomenclature

Φ	=	DMD modes
Λ	=	DMD eigenvalues
$\boldsymbol{\eta}$	=	spacecraft state vector
$\boldsymbol{x}$	=	vector of unmeasured states
$\boldsymbol{y}$	=	vector of measured states
$\boldsymbol{z}$	=	vector of mode amplitudes
C	=	observer matrix
C_x	=	observer matrix for $\boldsymbol{x}$
C_y	=	observer matrix for $\boldsymbol{y}$
F	=	state transition matrix for $\boldsymbol{z}$ dynamics
L	=	panel side length
$\boldsymbol{r}_i$	=	position of spacecraft component i
$\boldsymbol{v}_i$	=	velocity of spacecraft component i
R_i	=	Rotation matrix representation of attitude of spacecraft component i
$\boldsymbol{\omega}_i$	=	angular velocity of spacecraft component i
ζ_i	=	position of panel i in $\hat{\boldsymbol{a}}_3$ direction

I. Introduction

Recent advancements in space technology such as decreasing launch costs, deployable technology, and flexible materials, have facilitated the demand for larger spacecraft. Large spacecraft often possess inherent flexibilities that can be excited by maneuvers, leading to structural oscillations. These oscillations may pose problems to attitude control, cause structural damage, or degrade the intended function of the spacecraft. Effective mitigation of induced oscillations is crucial and can be approached in several ways.

One mitigation strategy involves using more sophisticated control laws to minimize structural excitation or to directly try to suppress induced oscillations. Research investigating vibration suppression includes a piezoelectric actuation

*Graduate student, Department of Aerospace Engineering, University of Maryland, College Park, MD, 20742
†Willis H. Young Jr. Professor of Aerospace Engineering Education, Department of Aerospace Engineering and Institute for Systems Research, University of Maryland, College Park, MD 20742. AIAA Senior Member

and associated robust control schemes as in [1, 2], control of actuators at the interface between connected elements of the spacecraft, [3], and distributed control moment gyros to counteract unwanted motion [4, 5]. However, in order for many of these control laws to be effectively applied, the shape of the spacecraft must be known. In the case of a deployable structure with connected segments, the state of each of the segments may be required for distributed control. However, if a high-dimensional state is needed to represent the structural dynamics, this can require an increasingly significant amount of computation power to perform state estimation. Due to the limited computation power available to a spacecraft in orbit and the need to perform estimation in real time, a high-dimensional state may make some of these types of control laws infeasible. In [6] an Eigensystem Realization Algorithm is used to generate a reduced-order model of a flexible spacecraft in order to estimate shape in real time, although it is focused primarily on modeling between input and output space which may not be sufficient for implementing control. To estimate the dynamics of a flexible spacecraft an adaptive scheme is used in [7] to learn unknown physical parameters of the spacecraft.

Modal decomposition encompasses a common class of methods for making algorithms on high-dimensional systems more computationally tractable. The goal of modal decomposition is to represent a high-dimensional system with a relatively small number of modes that capture the relevant behavior of the system. One method that has gained popularity, particularly in the field of fluid mechanics, is dynamic mode decomposition (DMD) [8]. DMD is a data-driven algorithm that was first developed for analyzing fluid flows. It is closely related to the Koopman operator, which is a way to represent a finite-dimensional nonlinear system as an infinite-dimensional linear system. The goal of DMD is to decompose data from time-series measurements into modes that capture the underlying dynamics of the system [9]. DMD may also be used to perform state estimation by using measurements of the system to estimate the DMD mode amplitudes using a Kalman filter, which can be used to estimate the full system state. This framework, described in [10], is referred to as the DMD Kalman filter and, if the DMD modes are an approximation of the Koopman modes, is equivalent to the Koopman-Kalman filter [10]. While DMD is popular in the field of fluid mechanics, it has not received the same level of attention or use in other fields. However, the model-order reduction and linear estimation framework it enables make it a promising approach to apply to shape estimation of flexible spacecraft.

The contributions of this paper are as follows: (1) a state-space representation of the dynamics of a spacecraft consisting of a hub and a flexible appendage modeled by a discretized set of flexibly connected elements; (2) the application of dynamic mode decomposition to the flexible spacecraft model to produce a reduced-order representation; and (3) using the reduced-order model to enable full state estimation with a limited set of measurements. State estimation of a flexible spacecraft using a reduced-order model enables complex flexible dynamics to be estimated in real time, which in turn enables monitoring and control of vibration.

The paper is organized as follows. Section II introduces dynamic mode decomposition and how a Kalman filter may be used to estimate mode amplitudes. Section III develops a three-dimensional dynamic model of a flexible spacecraft and how DMD is applied to the model. Section IV uses the Kalman filter to perform state estimation of the dynamic model and includes performance results. Section V summarizes the paper and ongoing and future work.

II. Preliminaries

A. Dynamic Mode Decomposition

Consider a sequence of evolving measurements arising from either simulated or experimental data. Each individual measurement is referred to as a snapshot and the the snapshots at time t_k are denoted $\chi(t_k)$. Assume that the time step between each snapshot is constant, i.e., $t_{k+1} - t_k = \Delta t$ for all k. If there are m snapshots, a matrix can be formed from these snapshots such that kth column corresponds to the vector of measurements at time k, i.e.,

$$X = \begin{bmatrix} | & | & & | \\ \chi(t_1) & \chi(t_2) & \dots & \chi(t_m) \\ | & | & & | \end{bmatrix}. \tag{1}$$

Next, two data matrices are formed from the sequence of snapshots such that the kth column in the second matrix corresponds to the advancement in time of the kth column of the first matrix by Δt.

$$X_0 = \begin{bmatrix} | & | & & | \\ \chi(t_1) & \chi(t_2) & \dots & \chi(t_{m-1}) \\ | & | & & | \end{bmatrix} \tag{2}$$

$$X_1 = \begin{bmatrix} | & | & & | \\ \chi(t_2) & \chi(t_3) & \dots & \chi(t_m) \\ | & | & & | \end{bmatrix} \tag{3}$$

The goal of dynamic mode decomposition is to find an eigendecomposition of the matrix A that linearly approximates the evolution of the dynamics of the system by one time step Δt, i.e,. $X_1 = AX_0$. The best fit in the least-squares sense for A can be computed using the psuedoinverse denoted $\dagger$, i.e., $A = X_1 X_0^\dagger$. However, if the dimension of X_0 is very large, this may become unreasonable to compute. Instead, the singular value decomposition (SVD) of X_0 is taken, i.e.,

$$X_0 = U\Sigma V^* \tag{4}$$

where $*$ denotes the conjugate transpose. The psuedoinverse of the SVD may be taken as $X_0^\dagger = V\Sigma^{-1}U^*$, yielding

$$A = X_1 V\Sigma^{-1}U^*. \tag{5}$$

An optimal low-dimensional representation of A denoted $\tilde{A}$ defined by the columns of U is [8]

$$\tilde{A} = U^*AU = U^*X_1V\Sigma^{-1}. \tag{6}$$

Let Λ be the eigenvalues of $\tilde{A}$ in matrix form and W the matrix of right eigenvectors of $\tilde{A}$. The DMD eigenvalues are given by Λ and the DMD modes given by [8]

$$\Phi = UW. \tag{7}$$

Let $\alpha(t_k)$ represent the mode amplitudes of the vector snapshot $\chi(t_k)$ in the DMD basis, i.e., $\chi(t_k) \approx \Phi\alpha(t_k)$. Then the approximate solution for the time evolution of snapshots can be reconstructed by [8]

$$\chi(t_k) \approx \Phi\Lambda^{(t_k - t_1)/\Delta t}\alpha(t_1) \tag{8}$$

The degree to which the DMD modes and eigenvalues represent the system dynamics depends on the linearity of the system. If the system is linear, only the mode amplitudes depend on the initial condition and the system dynamics may be accurately reconstructed via Eq. (8). The more nonlinear the system is, the more that the modes and eigenvalues obtained via DMD will also depend on the initial condition of the dataset [11].

B. Mode Amplitude Kalman Filter

According to the Koopman observer framework [10], a subset of measurements from the system can be utilized in conjunction with the DMD modes in a linear observer to estimate the mode amplitudes of the DMD representation. These estimated amplitudes can be then used to reconstruct the complete state of the original system. This process is performed as follows.

Consider a matrix C that is formed from the columns of the DMD modes Φ [10]

$$\begin{aligned} C_i &= \boldsymbol{\phi}_i \big\} && \text{if } \boldsymbol{\phi}_i \text{ is real} \\ C_i &= \mathrm{Re}(\boldsymbol{\phi}_i) \Big\} && \text{if } \boldsymbol{\phi}_i \text{ and } \boldsymbol{\phi}_{i+1} \text{ are complex conjugates.} \\ C_{i+1} &= \mathrm{Im}(\boldsymbol{\phi}_i) \Big\} \end{aligned} \tag{9}$$

Let $\boldsymbol{z}_k$ denote a vector of DMD mode amplitudes. The state $\boldsymbol{\eta}_k$ of the underlying system at timestep k can be estimated from the mode amplitudes by

$$\hat{\boldsymbol{\eta}}_k \approx C\boldsymbol{z}_k. \tag{10}$$

Consider also a block diagonal matrix F that is formed from the DMD eigenvalues [10] such that F has a diagonal entry $F_{i,i} = \lambda_i$, if λ_i is real, and block diagonal entry

$$\begin{bmatrix} F_{i,i} & F_{i,i+1} \\ F_{i+1,i} & F_{i+1,i+1} \end{bmatrix} = \begin{bmatrix} \mathrm{Re}(\lambda_i) & \mathrm{Im}(\lambda_i) \\ -\mathrm{Im}(\lambda_i) & \mathrm{Re}(\lambda_i) \end{bmatrix} \tag{11}$$

if λ_i and λ_{i+1} are complex conjugates. The matrix F represents a linear operator that advances the vector of mode amplitudes $\boldsymbol{z}_k$ forward in time by one timestep, i.e.,

$$\boldsymbol{z}_k = F\boldsymbol{z}_{k-1}. \tag{12}$$

The matrices Eqs. (10) and (12) define a linear dynamical system where the state is the DMD mode amplitudes and the observation is the state of the underlying system. Assume also that only some subset of the state of the underlying system is measured. Let $\boldsymbol{y}_k \in \mathbb{R}^{n_x}$ denote the portion of the state vector that is measured and $\boldsymbol{x}_k \in \mathbb{R}^{n_y}$ denote the portion that is to be estimated. The state vector $\boldsymbol{\eta}$ is reordered such that the observed portion of the state is partitioned from the unobserved portion of the state [10], i.e.,

$$\boldsymbol{\eta}_k = \begin{bmatrix} | \\ \boldsymbol{y}_k \\ | \\ \boldsymbol{x}_k \\ | \end{bmatrix}. \tag{13}$$

Note that when performing DMD, the snapshot matrix containing the training data must similarly be reordered.

$$X = \begin{bmatrix} | & | & & | \\ \boldsymbol{y}(t_1) & \boldsymbol{y}(t_2) & \dots & \boldsymbol{y}(t_m) \\ | & | & & | \\ \boldsymbol{x}(t_1) & \boldsymbol{x}(t_2) & \dots & \boldsymbol{x}(t_m) \\ | & | & & | \end{bmatrix}. \tag{14}$$

The C matrix is reordered the same way and partitioned such that the first n_y rows corresponding to the measured states are denoted C_y and the remaining n_x row corresponding to the unmeasured states are denoted C_x. The linear dynamical system may now be written as [10]

$$\boldsymbol{z}_k = F\boldsymbol{z}_{k-1} \tag{15a}$$
$$\boldsymbol{y}_k \approx C_y\boldsymbol{z}_k \tag{15b}$$
$$\boldsymbol{x}_k \approx C_x\boldsymbol{z}_k \tag{15c}$$

If the system given by Eq. (15) is observable, then a state observer may be applied to estimate the DMD mode amplitudes. For a linear system subject to Gaussian process and measurement noise, the Kalman filter represents an optimal observer. Consequently, a Kalman filter may be used to estimate the mode amplitude amplitudes given a set of measurements of the underlying system. The Kalman filter of the mode amplitudes is as follows [12]:

Estimate propagation:

$$\hat{\boldsymbol{z}}_{\bar{k}} = F\hat{\boldsymbol{z}}_{k-1} \tag{16}$$
$$P_{\bar{k}} = FP_{k-1}F^T + Q \tag{17}$$
$$\tag{18}$$

Kalman Gain:

$$K_k = P_{\bar{k}}C_y\left(C_yP_{\bar{k}}C_y^T + R\right)^{-1} \tag{19}$$

Measurement assimilation:

$$\hat{z}_k = \hat{z}_{\bar{k}} + K(\boldsymbol{y}_k - C_y \hat{z}_{\bar{k}}) \tag{20}$$

$$P_k = (I - KC_y)P_{\bar{k}} \tag{21}$$

Estimate of $\boldsymbol{x}$:

$$\hat{\boldsymbol{x}}_k = C_x \hat{z}_k \tag{22}$$

where $\bar{}$ denotes an a priori estimate. The DMD Kalman filter provides a framework for generating a reduced-order model of a system and enabling state estimation with a limited subset of measurements [10].

III. Dynamic Mode Decomposition of a Flexible Spacecraft

This section derives the modeling of a flexible spacecraft and applies the DMD algorithm to the proposed model to yield a modal decomposition. The projection error as a function of the number of modes used in the decomposition is also examined.

A. Flexible Spacecraft Model

Consider a spacecraft consisting of a hub and a large flexible appendage connected to the hub. This appendage could represent a large solar array, antenna, solar sail, or other relevant structure. To model the flexibility of the structure, assume that the appendage is modeled as a discretized set of flexibly connected rigid square elements referred to as panels. This modeling choice can represent a deployable structure that is folded for launch and deployed in space, but by varying the size of the panel discretization and the flexibility of the panel connections, can be generalized to represent a continuous flexible planar structure.

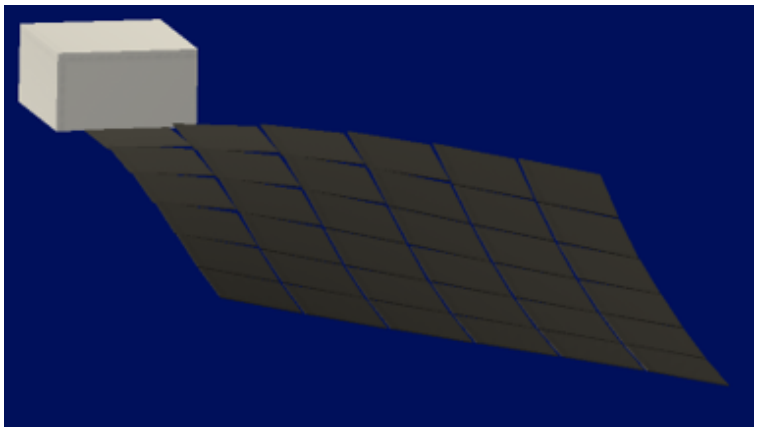

Fig. 1 Spacecraft with a hub and a flexible appendage modeled as N flexibly connected panels

Consider an Earth-centered inertial frame $\mathcal{I} = (O, \hat{\mathbf{e}}_x, \hat{\mathbf{e}}_y, \hat{\mathbf{e}}_3)$, a body-fixed frame affixed to the central hub of the spacecraft $\mathcal{A} = (C, \hat{\mathbf{a}}_1, \hat{\mathbf{a}}_2, \hat{\mathbf{a}}_3)$, and body-fixed frames affixed to each of the component panels of the appendage $\mathcal{B}^{(i)} = (B^{(i)}, \hat{\mathbf{b}}_1^{(i)}, \hat{\mathbf{b}}_2^{(i)}, \hat{\mathbf{b}}_3^{(i)})$, $i = 1, ..., N$. The panels are assumed to all be the same size with side length L, and their body-fixed reference frames are such that the origin is at the center of the panel, and the 1 and 2 axes are aligned with the panel edges.

The state of the hub consists of its position, velocity, attitude, and angular velocity, i.e.,

$$\boldsymbol{\eta}_C = \begin{bmatrix} \mathbf{r}_{C/O} & \mathbf{v}_{C/O} & R_C & \boldsymbol{\omega}_C \end{bmatrix}^T, \tag{23}$$

where the attitude is represented by a rotation matrix. To better capture the shape of the flexible appendage with the states of the panels, the position and velocity of the panels relative to and in the reference frame of the hub are used, i.e.,

$$\boldsymbol{\eta}_i = \begin{bmatrix} \mathbf{r}_{i/C} & \mathbf{v}_{i/C} & R_{B_i} & \boldsymbol{\omega}_{B_i} \end{bmatrix}^T. \tag{24}$$

The state of the full spacecraft model is then a concatenation of the hub and all panels making up the appendage, i.e.,

$$\boldsymbol{\eta} = [\boldsymbol{\eta}_C \quad \boldsymbol{\eta}_1 \quad \boldsymbol{\eta}_2 \quad \dots \quad \boldsymbol{\eta}_N]^T, \tag{25}$$

where N is the number of elements composing the appendage.

Spacecraft Dynamics

The dynamics for the state of the hub are as follows:

$$\dot{\mathbf{r}}_{C/O} = \dot{\mathbf{v}}_{C/O} \tag{26}$$

$$\dot{\mathbf{v}}_{C/O} = \frac{\boldsymbol{F}_C}{m_C} \tag{27}$$

$$\dot{R}_C = R_C \boldsymbol{\omega}_C^{\times} \tag{28}$$

$$J_C \dot{\boldsymbol{\omega}}_C = -\boldsymbol{\omega}_C^{\times} J_C \boldsymbol{\omega}_C + \boldsymbol{M}_C \tag{29}$$

where the $^{\times}$ operator is a mapping from $\mathbb{R}^3$ to a 3×3 skew-symmetric matrix such that $a^{\times} b = a \times b$ and where $\boldsymbol{\tau}_C$ is the total external torque experienced by the hub and the derivatives are taken with respect to the inertial frame.

To derive the dynamics of each panel in the reference frame of the hub, the inertial frame dynamics must first be considered. The position of panel i in the inertial frame is

$$\mathbf{r}_{i/O} = \mathbf{r}_{C/O} + \mathbf{r}_{i/C}. \tag{30}$$

Differentiating twice yields the acceleration of each panel in the inertial frame, i.e.,

$$\boldsymbol{a}_{i/O} = \boldsymbol{a}_{C/O} + \boldsymbol{a}_{i/C} + \dot{\boldsymbol{\omega}}_C \times \boldsymbol{r}_{i/C} + 2\boldsymbol{\omega}_C \times \boldsymbol{v}_{i/C} + \boldsymbol{\omega}_C \times (\boldsymbol{\omega}_C \times \boldsymbol{r}_{i/C}). \tag{31}$$

Rearranging and substituting in $\boldsymbol{F}_C = m_C \boldsymbol{a}_C$ and $\boldsymbol{F}_i = m_i \boldsymbol{a}_i$, where $\boldsymbol{F}_C$ and $\boldsymbol{F}_i$ are the total forces on the hub and ith panel, respectively, yields

$$\boldsymbol{a}_{i/C} = \frac{\boldsymbol{F}_i}{m_i} - \frac{\boldsymbol{F}_C}{m_C} - \dot{\boldsymbol{\omega}}_C \times \boldsymbol{r}_{i/C} - 2\boldsymbol{\omega}_C \times \boldsymbol{v}_{i/C} - \boldsymbol{\omega}_C \times (\boldsymbol{\omega}_C \times \boldsymbol{r}_{i/C}). \tag{32}$$

The dynamics for the ith panel are

$$\dot{\mathbf{r}}_{i/C} = \dot{\mathbf{v}}_{i/C} \tag{33}$$

$$\dot{\mathbf{v}}_{i/C} = \frac{\boldsymbol{F}_i}{m_i} - \frac{\boldsymbol{F}_C}{m_C} - \dot{\boldsymbol{\omega}}_C \times \boldsymbol{r}_{i/C} - 2\boldsymbol{\omega}_C \times \boldsymbol{v}_{i/C} - \boldsymbol{\omega}_C \times (\boldsymbol{\omega}_C \times \boldsymbol{r}_{i/C}) \tag{34}$$

$$\dot{R}_{B_i} = R_{B_i} \boldsymbol{\omega}_{B_i}^{\times} \tag{35}$$

$$J_{B_i} \dot{\boldsymbol{\omega}}_{B_i} = -\boldsymbol{\omega}_{B_i}^{\times} J_{B_i} \boldsymbol{\omega}_{B_i} + \boldsymbol{M}_i \tag{36}$$

Internal Force and Moment Model

Assume that each of the panels are connected to each adjacent panel and at each connection there is a torsional spring that generates a restoring moment for adjacent panels with offset attitudes. In order to avoid the unnecessary complexities associated with explicitly considering the panel connections as constraints, the attachment force of each panel is modeled as a stiff damped spring with spring coefficient k_s and damping coefficient c_s. Assume the torsional springs at adjacent panels are linearly proportional to the relative angle between the panels that it connects, with spring coefficient k_t and damping coefficient c_t. With the spring modeling, the attachment force and resulting moment between two adjacent panels can be computed from the relative position and velocity of the panel edges. The position of an edge in a panel's reference frame is

$$\mathbf{L} = \pm \begin{bmatrix} \frac{L}{2} & 0 & 0 \end{bmatrix} \quad \text{or} \quad \pm \begin{bmatrix} 0 & \frac{L}{2} & 0 \end{bmatrix}. \tag{37}$$

The relative position between the edges of two adjacent panels i and j is

$$\mathbf{r}_{i,j/\text{edge}} = \mathbf{r}_{i/C} + R_{C/B_i} \mathbf{L} - (\mathbf{r}_{j/C} - R_{C/B_i} \mathbf{L}), \tag{38}$$

where R_{C/B_i} is the rotation matrix from B_i to C computed by $R_{C/B_i} = R_C^T R_{B_i}$. The relative velocity between the edges of panels i and j is derived by taking the derivative of $\mathbf{r}_{i,j/\text{edge}}$, which yields

$$\mathbf{v}_{i,j/\text{edge}} = \mathbf{v}_{i/C} + R_{C/B_i}(\boldsymbol{\omega}_i - R_{B_i/C}\boldsymbol{\omega}_C) \times \mathbf{L} - (\mathbf{v}_{j/C} + R_{C/B_i}(\boldsymbol{\omega}_j - R_{B_i/C}\boldsymbol{\omega}_C) \times (-\mathbf{L})). \tag{39}$$

The force on panel i resulting from panel j is

$$\mathbf{F}_{i,j} = -k_s \mathbf{r}_{i,j/\text{edge}} - c_s \mathbf{v}_{i,j/\text{edge}}, \tag{40}$$

where $\boldsymbol{F}_{j,i} = -\boldsymbol{F}_{i,j}$. The moment on i resulting from the attachment with j is

$$\mathbf{T}_{i,j} = \mathbf{L} \times (R_{B_i/C}\mathbf{F}_{i,j}). \tag{41}$$

Similarly, the moment arising from the torsional spring between two adjacent panels is computed from the relative attitude and angular velocity of adjacent panels. Assume that the restoring moment opposes the relative orientation of adjacent panels. The matrix logarithm of a rotation matrix parameterizes a rotation in three-dimensional space by a direction $\boldsymbol{\xi}$ and magnitude θ of rotation providing a convenient way to define the magnitude and direction of the restoring moment induced by the torsional spring. The matrix logarithm of a rotation matrix R is

$$\text{logm}(R) = \begin{cases} \theta = \cos^{-1}(\frac{\text{Trace}(R)-1}{2}) \in \mathbb{R} \\ \boldsymbol{\xi} = \frac{1}{2\sin\theta}\begin{bmatrix} r_{32} - r_{23} \\ r_{13} - r_{31} \\ r_{21} - r_{12} \end{bmatrix} \in \mathbb{R}^3 \end{cases} \tag{42}$$

The relative orientation between adjacent panels i and j is computed by taking $\text{logm}(R_{B_i/B_j})$ to get $\theta_{i,j}$ and $\boldsymbol{\xi}_{i,j}$. The relative angular velocity between adjacent panels i and j is the difference between their angular velocities given in reference frame B_i, i.e.,

$$\boldsymbol{\omega}_{i,j} = \boldsymbol{\omega}_i - R_{B_i/B_j}\boldsymbol{\omega}_j. \tag{43}$$

The resulting moment is

$$\mathbf{M}_{i,j} = -k_t\theta\boldsymbol{\xi}_{i,j} - c_t\boldsymbol{\omega}_{i,j}. \tag{44}$$

Assume that the spacecraft is subject to gravity from Earth, that there is some 3-axis control system on the hub, e.g., a set of reaction wheels, and that the appendage is connected to the hub via a single panel indexed $i = 1$. Then the total force and moment exerted on the hub via the flexible appendage is

$$\boldsymbol{F}_C = -\mu m_C \frac{\mathbf{r}_{C/O}}{\|\mathbf{r}_{C/O}\|^3} + \boldsymbol{F}_{C,1} \tag{45}$$

$$\boldsymbol{M}_C = \boldsymbol{T}_{C,1} + \boldsymbol{M}_{C,1} + \boldsymbol{u}_C. \tag{46}$$

The total force and moment on each panel comprising the appendage is

$$\boldsymbol{F}_i = -\mu m_i \frac{\mathbf{r}_{i/O}}{\|\mathbf{r}_{i/O}\|^3} + \sum_{j\in\mathcal{N}_i} \boldsymbol{F}_{i,j} \tag{47}$$

$$\boldsymbol{M}_i = \sum_{j\in\mathcal{N}_i} \left(\boldsymbol{T}_{i,j} + \boldsymbol{M}_{i,j}\right), \tag{48}$$

where $\mathcal{N}_i$ is the set of all panels connected to panel i. Consider the term $\frac{\boldsymbol{F}_i}{m_i} - \frac{\boldsymbol{F}_C}{m_C}$ appearing in the translational dynamics 32 of each panel. Substituting the total forces into this expression yields

$$\frac{\boldsymbol{F}_i}{m_i} - \frac{\boldsymbol{F}_C}{m_C} = -\mu\frac{\mathbf{r}_{i/O}}{\|\mathbf{r}_{i/O}\|^3} + \mu\frac{\mathbf{r}_{C/O}}{\|\mathbf{r}_{C/O}\|^3} + \frac{1}{m_i}\sum_{j\in\mathcal{N}_i}\boldsymbol{F}_{i,j} - \frac{1}{m_C}\boldsymbol{F}_{C,1}. \tag{49}$$

For a large spacecraft, the difference between $\mathbf{r}_{i/O}$ and $\mathbf{r}_{C/O}$ might be on the order of 10s of meters at most while their magnitude is on the order of thousands of kilometers. Consequently, the gravitational influence on each term

differs minimally, allowing for the approximation $\mathbf{r}_{i/O} \approx \mathbf{r}_{C/O}$. As a result, the gravitational contributions cancel out in Eq. (49), i.e.,

$$\frac{\boldsymbol{F}_i}{m_i} - \frac{\boldsymbol{F}_C}{m_C} \approx \frac{1}{m_i} \sum_{j \in \mathcal{N}_i} \boldsymbol{F}_{i,j} - \frac{1}{m_C} \boldsymbol{F}_{C,1} \tag{50}$$

Any relative acceleration between panel i and the hub induced by the differing gravitational forces is negligible compared to the system's structural dynamics. With this approximation, the dynamics of the appendage no longer depend on the inertial position and velocity of the spacecraft. As a result, the attitude and shape of the flexible spacecraft can be written as a state-space system independent of the translational dynamics of the hub. The state of this reduced system is

$$\boldsymbol{\eta} = [R_C \quad \boldsymbol{\omega}_C \quad \boldsymbol{\eta}_1 \quad \boldsymbol{\eta}_2 \quad \dots \quad \boldsymbol{\eta}_N]^T \tag{51}$$

and its dynamics can be written entirely as a function of its state, i.e.,

$$\dot{\boldsymbol{\eta}} = \boldsymbol{f}(\boldsymbol{\eta}). \tag{52}$$

This reduced state that represents the attitude and shape of the flexible spacecraft is considered for estimation.

B. Modal Decomposition of Spacecraft Model

To perform DMD on the flexible spacecraft model, a training dataset is required. To generate training data, a time-varying control input profile is applied to the system via $\boldsymbol{u}_C(t)$ for some amount of time, and the resulting unforced dynamics are measured and collected as a training dataset. For DMD to accurately capture the behavior of the underlying system, it is important that the training data contain all relevant modes. Because different magnitudes and frequencies of the control input will excite different modes of the structure, using a single set of data would likely not yield a representative modal decomposition. To mitigate this, many different datasets resulting from varying control input profiles were collected. These datasets were concatenated to form a single dataset that ideally reflects all the relevant modes of the system to which can DMD can be applied.

The training dataset is generated in simulation via a Monte Carlo approach as follows: (1) a control input profile bounded in magnitude and time is randomly generated and applied to the system; (2) the resulting unforced dynamic response is measured and collected for the subsequent 1200 seconds (about a fifth of a period of a low Earth orbit). This procedure is performed a number of times and each of the resulting datasets is concatenated together.

Training datasets were generated for a spacecraft model with two different discretization sizes of the flexible appendage. In both cases, the flexible appendage is a 15 meter by 15 meter square structure. The coarse discretization consists of a 6x6 grid of larger panels, whereas the finer discretization consists of an 18x18 grid of smaller panels. The snapshot matrices are constructed from the compiled training data and DMD was performed via the procedure described in Section II.A to obtain a modal decomposition for each discretization size. To rank the relative importance of each mode, the procedure described in [13] computing projection coefficients over all snapshot data is applied here. The 9 mode shapes of the appendage that contribute most to the system's response for each discretization are shown below. The hub is located at $(0, 0)$.

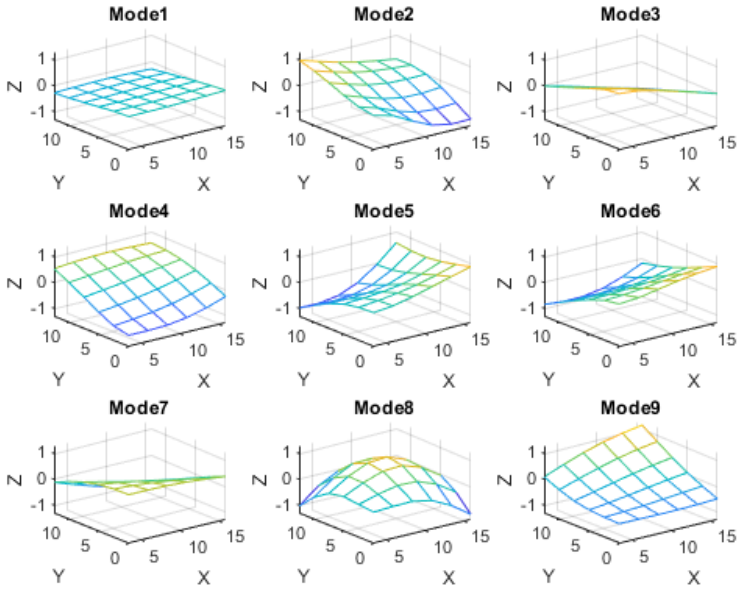

Fig. 2 First 9 modes of spacecraft model with the 6x6 discretization of the flexible appendage.

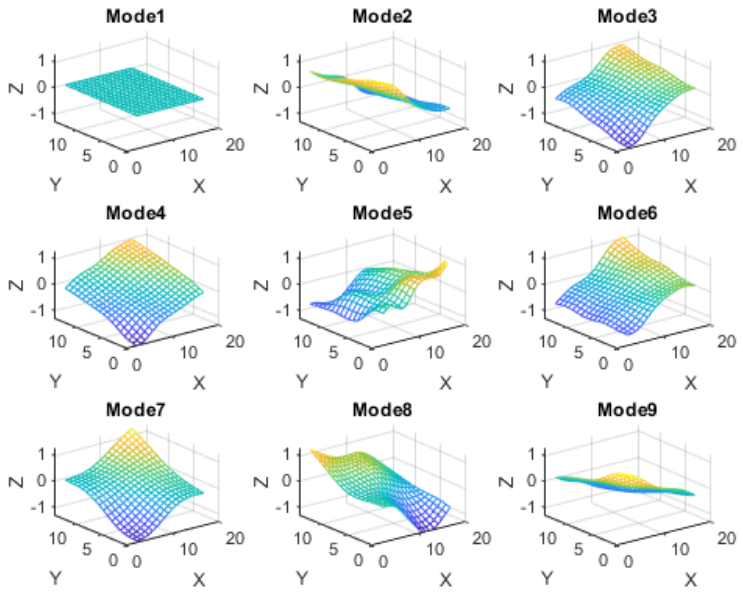

Fig. 3 First 9 modes of spacecraft model with the 18x18 discretization of the flexible appendage.

C. Impact of Mode Selection on Reconstruction Error

To evaluate how well the decomposition captures the underlying behavior of the system, dynamics of the spacecraft model from an initial condition separate from any in the training dataset can be projected onto the DMD modes. The projection, defined by $\hat{\boldsymbol{\eta}} = CC^{\dagger}\boldsymbol{\eta}$ is used to quantify the information lost due to projecting onto a lower-dimensional model. A separate dataset is generated using the same procedure as before and the projection computed. To compute

the error of a projection compared to the actual state, the following metrics are used. For position, the distance between the projected and actual position of an element is

$$\varepsilon_{r_i} = ||\tilde{r}_i - r_i||. \tag{53}$$

For velocity, the magnitude of the difference in the projected and actual velocity vectors of an element is

$$\varepsilon_{v_i} = ||\tilde{v}_i - v_i||. \tag{54}$$

For attitude, the angle between the attitudes of the actual and projection is

$$\varepsilon_{R_i} = \cos^{-1} \frac{\mathrm{Tr}(\hat{R}_i^T R_i) - 1}{2}. \tag{55}$$

For angular velocity, the magnitude of the difference between the actual and projected angular velocity is

$$\varepsilon_{\omega_i} = ||\tilde{\omega}_i - \omega_i||. \tag{56}$$

To quantify the projection error for each type of panel state (position, velocity, attitude, and angular velocity), the root mean square (RMS) error for each is taken over time and averaged over all the panels comprising the appendage. The results are shown in Fig. 4. To quantify error with a single quantity, a normalized root mean square error (NRMSE) metric is used. The error for each state type is normalized by the maximum of the absolute value of the measured values of that state type for the simulation, i.e., for position

$$r_{\mathrm{err}} = \frac{1}{N} \sum_{i=1}^{N} \frac{\|\tilde{\boldsymbol{r}}_i - \boldsymbol{r}_i\|}{\max(|\boldsymbol{r}_i|)}. \tag{57}$$

The normalized quantities for position, velocity, attitude, and angular velocity are summed to represent the total projection error of a simulation.

The sum and contribution of each state type is shown in Fig. 5. These metrics illustrate the effect of using different numbers of modes to represent the system dynamics. The resulting number of modes represents a significant reduction in the size of the original state-space model, which has 660 states.

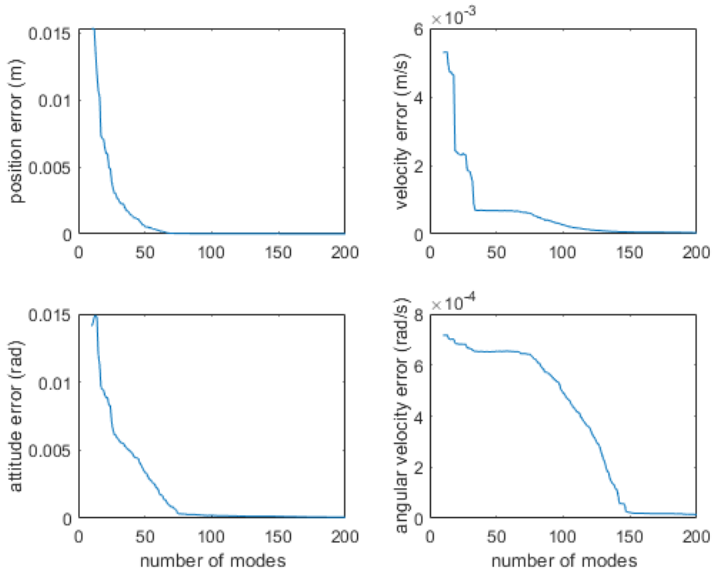

Fig. 4 Projection error of the position, velocity, attitude, and angular velocity resulting from using varying numbers of DMD modes to represent the underlying system dynamics.

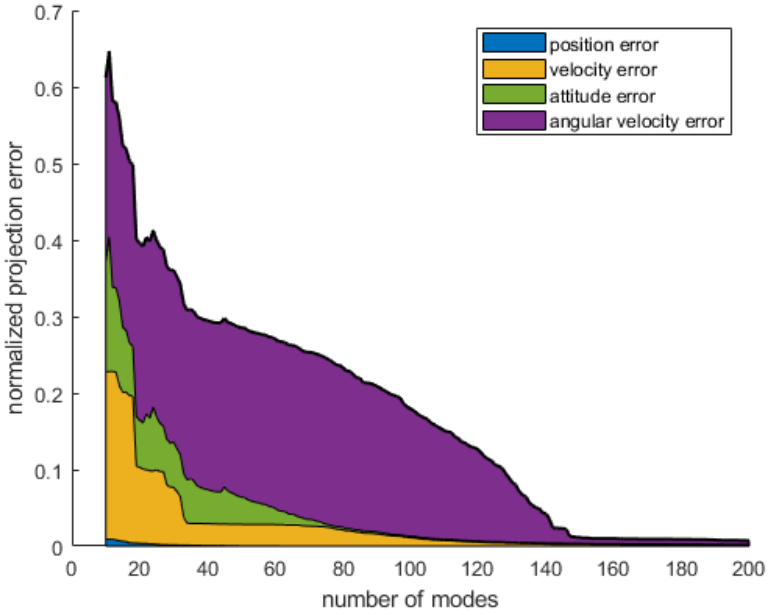

Fig. 5 Normalized projection error resulting from using varying numbers of DMD modes to represent the underlying system dynamics.

The projection error results show that differing numbers of modes are required for different state quantities. For example, with about 50 modes, the position of each panel can be almost fully recovered from the reduced order model. For angular velocity, about 150 modes are required for minimal projection loss. In the sum of normalized errors, the angular velocity contributes most to the total error. There are also two elbows occurring around 50 and 150 modes. Until around 50 modes, significantly less error is incurred with each additional mode added. At 150 modes, there is very little benefit to adding additional modes.

To assess whether the decomposition described in Section III.B captures all relevant modes, the total projection error resulting from different initial conditions can be compared. total projection error is computed using the same procedure. If the decomposition is representative, the total error across a variety of samples should only vary by small magnitudes. However, if certain initial conditions result in significantly larger projection errors than others, it suggests that those initial conditions may be exciting a mode not captured by the modal decomposition. To conduct this evaluation, simulations were conducted across 150 samples of randomly generated initial conditions. The Monte Carlo-generated modal decomposition, using a fixed number of modes, is then employed to compute the total projection error for each simulation. The results are presented in a histogram illustrating the distribution of projection errors, as shown in Fig. 6. The standard deviation of the projection error is 7.25×10^{-5}. The extremely small variance in projection error suggests that the modal decomposition successfully captures all relevant modes of the system. Additionally, this consistency in error distribution provides evidence that the underlying structural dynamics can be accurately represented as linear.

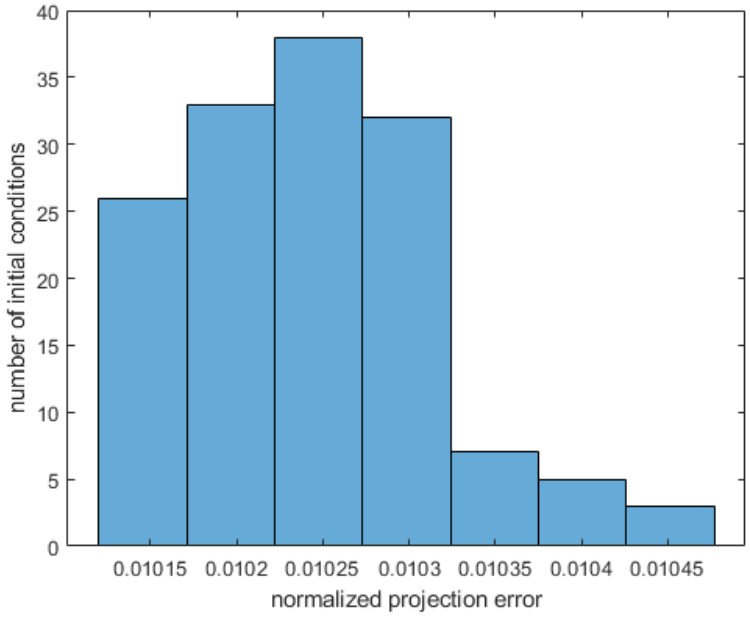

Fig. 6 Normalized projection error resulting from using varying numbers of DMD modes to represent the underlying system dynamics.

IV. State Estimation via a Mode Amplitude Kalman Filter

In this section, a DMD Kalman filter shown in Section II.B is applied to the flexible spacecraft model to perform state estimation given a limited set of measurements. A measurement function is proposed and numerical simulations are performed to evaluate the performance of the observation.

Assume that there are sensors on the hub that measure the attitude and angular velocity of the hub. Assume also that there is a sensor package such as an optical sensor on the hub or some array of differential GPS sensors distributed across the appendage that capture the shape deformation of the appendage. Specifically, assume that the relative offset of a subset of the panels along the $\hat{\boldsymbol{a}}_3$ axis, i.e., $\zeta_i = \boldsymbol{r}_{i/C} \cdot \hat{\boldsymbol{a}}_3$, is measured. If there are M panels measured, the measurement vector of the system is

$$\boldsymbol{y} = \begin{bmatrix} \boldsymbol{\eta}_C & \zeta_{\mathcal{M}_1} & \cdots & \zeta_{\mathcal{M}_M} \end{bmatrix}^T, \tag{58}$$

where $\mathcal{M}$ is the set of panels that are measured and M is the cardinality of $\mathcal{M}$.

To perform state estimation, the unforced dynamics of the system are simulated in response to an angular impulse imparted by the reaction wheels. The modal decomposition shown in Section III.B generates the mode amplitude state transition matrix F and observation matrix C. The initial state estimate assumes that the initial state of the appendage is flat and unmoving relative to the hub. Other simulation parameters are shown the appendix. The DMD Kalman filter algorithm is then applied to the measurements of the test simulation data to estimate the mode amplitudes from the shape measurements in Eq. (58), which in turn are used to estimate the full state of the system. To evaluate the effect of model reduction on the quality of the resulting state estimate, the elbows shown in Fig. 5 at 50 and 150 modes are selected to represent the system. For each discretization size, the measurements are taken at the same locations on the appendage. For the 6x6 discretization, $\mathcal{M}$ is selected to be all 36 panels. For the 18x18 discretization, $\mathcal{M}$ corresponds to measuring the center panel in each 3x3 group of panels. The spacecraft parameters for each discretization size and the parameters used for the DMD Kalman filter are shown in the appendix. Gaussian measurement noise with a standard deviation of 0.5 cm is applied to the panel measurements.

To quantify the performance of the DMD Kalman filter, the state estimate is compared to the true state values. The same metrics as in Eqs. (53) to (56) are used (with the state estimate instead of the projected state) to quantify the state estimate error. Specifically, the magnitude of the difference in position, velocity, and angular velocity between the estimated and real states and the angle between the real and estimated attitude estimate are computed and averaged over

each panel. The results are shown in Fig. 7 for the coarse discretization and Fig. 8 for the fine discretization. The total normalized error is again computed by normalizing each of these quantities by the maximum measured value as in Eq. (57). The procedure is applied to the position, velocity, attitude, and angular velocity estimates, and the normalized quantities are summed. The summed normalized error plots are shown in Fig. 9a and Fig. 9b.

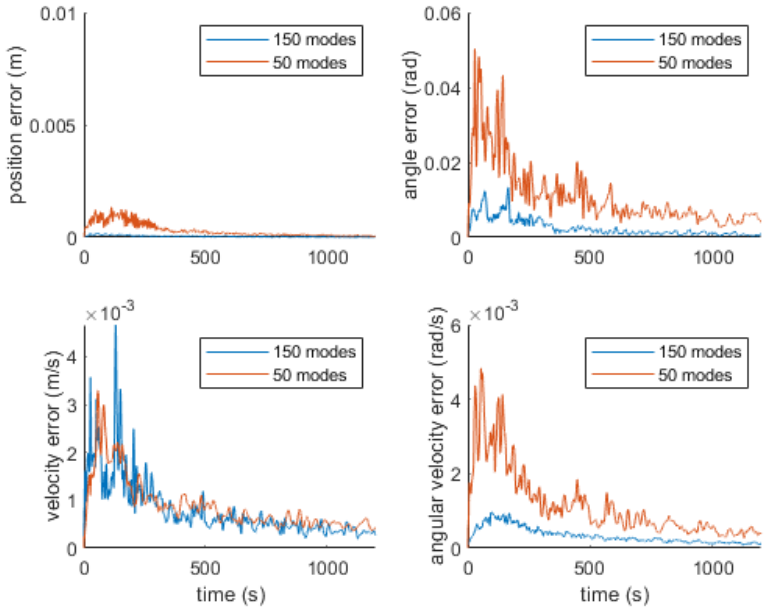

Fig. 7 Average estimation error of the position, velocity, attitude, and angular velocity of each panel for the 6x6 discretization of the flexible appendage.

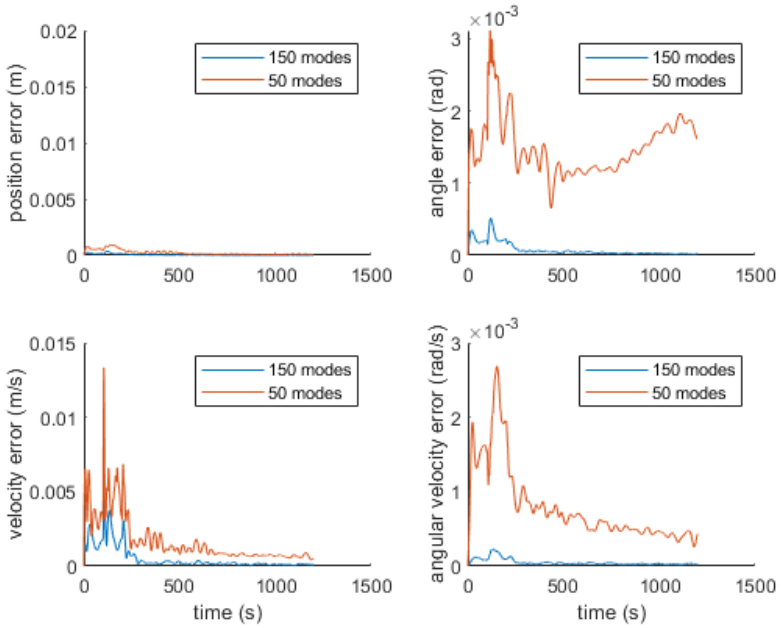

Fig. 8 Average estimation error of the position, velocity, attitude, and angular velocity of each panel for the 18x18 discretization of the flexible appendage.

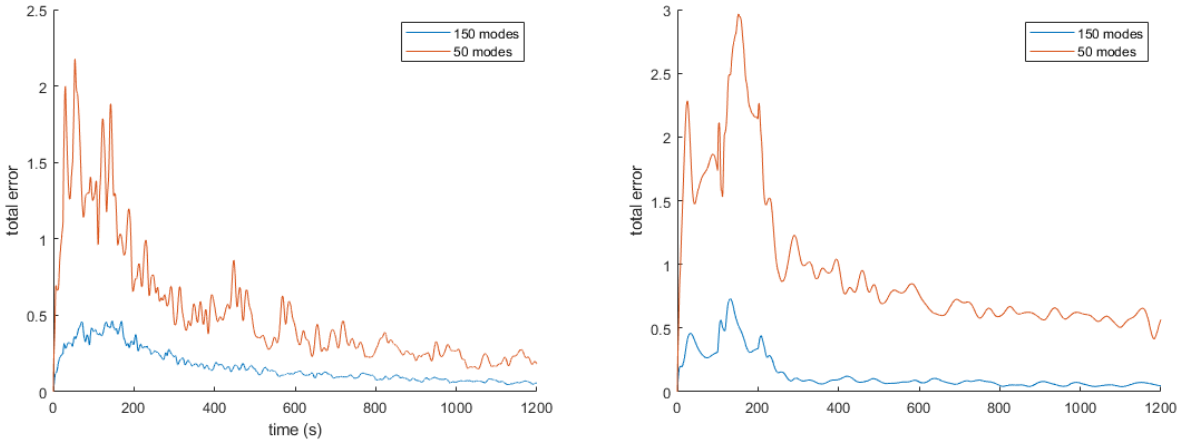

(a) 6x6 discretization **(b) 18x18 discretization**

Fig. 9 Normalized estimation error of the state of each panel of the flexible appendage compared using 50 and 150 modes for the (a) 6x6 discretization and (b) 18x18 discretization.

The results demonstrate that the estimator is able to reconstruct the states accurately, particularly when using 150 modes. For 150 modes, the position error is on the order of millimeters, the velocity error is on the order of millimeters per second, the attitude error is on the order of hundredths of a radian, and the angular velocity error is on the order of milliradians per second.

The difference in performance between the number of modes in estimation corresponds to what is seen in the projection error in Fig. 4. For position and velocity, the projection error suggests only marginal improvement going from 50 to 150 modes, whereas in attitude and angular velocity, the improvement is more substantial. This is seen in the estimation error, as the estimation of attitude and angular velocity improves more significantly by increasing to 150 modes.

Impact of Model Fidelity and Mode Number on Computation Time

The results from Section IV also suggest that despite using a finer discretization, the estimator is able to accurately estimate the underlying dynamics with a similar number of modes as the coarser discretization. Consequently, the computation savings from using DMD to perform state estimation becomes more valuable the larger the original state size is. For the 6x6 discretization, there are 660 states, which can be represented using 150 modes and both can be estimated using 36 measurements. For the 18x18 discretization, there are 5844 states, which also can be represented using 150 modes and estimated with only 36 measurements. Whereas estimation of such a high-degree system in real time on space hardware would be computationally infeasible, the computational burden is significantly reduced using DMD and the DMD Kalman filter. To illustrate the comparison of performance versus computation time and steady state error, the computation time to perform state estimation for the 1200 second simulation on a Dell Precision 3570 laptop with an Intel Core i5-1235U processor is shown in Fig. 10.

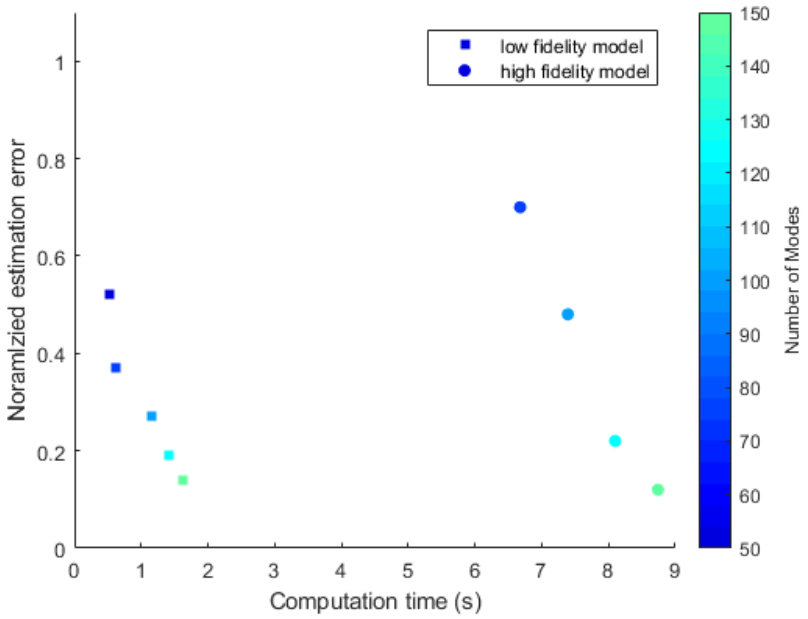

Fig. 10 Computation time compared with performance of state estimation across different modes and discretization sizes

V. Conclusion

This paper proposes a dynamic spacecraft model consisting of a hub and flexible appendage modeled by a discretized series of flexibly connected rigid elements. Using numerical simulation data, dynamic mode decomposition is performed yielding a modal representation of the system dynamics. A reduced-order model of the system is formed using the modal representation by selecting the most relevant modes. The impact of information lost using the reduced-order representation as a function of the number of modes selected is shown. The DMD Kalman filter is applied using the reduced order model to perform full state estimation. Numerical simulations demonstrate accurate state estimation with significantly reduced-order models, resulting in significant savings in computation time.

Ongoing work includes further characterizing the trade-off between computation time and performance using various numbers of modes and fidelity of appendage discretization. Additionally, with the linear dynamical system characterized by the mode amplitude state transition matrix and the observer matrix, observability may be computed for a given set of measurements. With this, one might determine various combinations of states that need to be measured to ensure that the system is observable. This information provides a spacecraft designer the type and number of sensors required to perform real time shape estimation. This idea may be extended by optimizing the location of sensors on the appendage according to the quality of state estimates a particular configuration can provide.

Appendix

Simulation Parameters

parameter	k_s	c_s	k_t	c_t	m_C	m_i	L
value	1000	5	0.1	0.05	1000	100	2.5
unit	$\frac{\text{N}}{\text{m}}$	$\frac{\text{Ns}}{\text{m}}$	$\frac{\text{Nm}}{\text{rad}}$	$\frac{\text{Nms}}{\text{rad}}$	kg	kg	m

Table 1 6x6 **simulation parameters**

parameter	k_s	c_s	k_t	c_t	m_C	m_i	L
value	1000	5	0.1	0.05	1000	11.11	0.83
unit	$\frac{\text{N}}{\text{m}}$	$\frac{\text{Ns}}{\text{m}}$	$\frac{\text{Nm}}{\text{rad}}$	$\frac{\text{Nms}}{\text{rad}}$	kg	kg	m

Table 2 18x18 **simulation parameters**

Estimation Parameters

$$Q = 0.1\ \mathcal{I}_{nmxnm}$$

$$R = \begin{bmatrix} 0.01\ \mathcal{I}_{9x9} & 0 \\ 0 & 0.1\ \mathcal{I}_{mxm} \end{bmatrix}$$

References

[1] Cao, X., Yue, C., and Liu, M., "Flexible satellite attitude maneuver via constrained torque distribution and active vibration suppression," *Aerospace Science and Technology*, Vol. 67, 2017, p. 387–397. https://doi.org/10.1016/j.ast.2017.04.014.

[2] Sun, J., Li, S., Huang, J., and Zhu, D., "Robust coordinated control for large flexible spacecraft based on consensus theory," *Journal of the Franklin Institute*, Vol. 357, No. 9, 2020, p. 5359–5379. https://doi.org/10.1016/j.jfranklin.2020.02.049.

[3] Zhang, Y., and Guan, X., "Active damping control of flexible appendages for spacecraft," *Aerospace Science and Technology*, Vol. 75, 2018, p. 237–244. https://doi.org/10.1016/j.ast.2017.12.027.

[4] Hu, Q., Jia, Y., and Xu, S., "Dynamics and vibration suppression of space structures with control moment gyroscopes," *Acta Astronautica*, Vol. 96, 2014, p. 232–245. https://doi.org/10.1016/j.actaastro.2013.11.032.

[5] Feng, X., Jia, Y., and Xu, S., "Dynamics of flexible multibody systems with variable-speed control moment gyroscopes," *Aerospace Science and Technology*, Vol. 79, 2018, p. 554–569. https://doi.org/10.1016/j.ast.2018.06.004.

[6] Brownell, M., Sinclair, A. J., and Singla, P., "A subspace method for shape estimation of flexible spacecraft membrane," *AIAA SCITECH 2022 Forum*, 2022. https://doi.org/10.2514/6.2022-2378.

[7] Woodward, N., and Bevilacqua, R., "Onboard estimation of unknown dynamics of flexible spacecraft," *Acta Astronautica*, Vol. 217, 2024, pp. 363–381. https://doi.org/https://doi.org/10.1016/j.actaastro.2024.01.042, URL https://www.sciencedirect.com/science/article/pii/S009457652400050X.

[8] Tu, J. H., Rowley, C. W., Luchtenburg, D. M., Brunton, S. L., and Kutz, J. N., "On dynamic mode decomposition: Theory and applications," *Journal of Computational Dynamics*, Vol. 1, No. 2, 2014, pp. 391–421. https://doi.org/10.3934/jcd.2014.1.391, URL https://www.aimsciences.org/article/id/1dfebc20-876d-4da7-8034-7cd3c7ae1161.

[9] Kutz, N. J., Brunton, S. L., Brunton, B. W., and Proctor, J. L., *Dynamic mode decomposition: Data-driven modeling of Complex Systems*, Society for industrial and applied mathematics, 2016.

[10] Surana, A., and Banaszuk, A., "Linear observer synthesis for nonlinear systems using Koopman Operator framework," *IFAC-PapersOnLine*, Vol. 49, No. 18, 2016, pp. 716–723. https://doi.org/https://doi.org/10.1016/j.ifacol.2016.10.250, URL https://www.sciencedirect.com/science/article/pii/S2405896316318304, 10th IFAC Symposium on Nonlinear Control Systems NOLCOS 2016.

[11] Gomez, D. F., Lagor, F. D., Kirk, P. B., Lind, A. H., Jones, A. R., and Paley, D. A., "Data-driven estimation of the unsteady Flowfield near an actuated airfoil," *Journal of Guidance, Control, and Dynamics*, Vol. 42, No. 10, 2019, p. 2279–2287. https://doi.org/10.2514/1.g004339.

[12] Crassidis, J. L., and Junkins, J. L., *Optimal Estimation of Dynamic Systems*, CRC Press, 2012.

[13] Rot, M., Horvat, M., and Kosec, G., "Dynamic mode decomposition as an analysis tool for time-dependent partial differential equations," *2022 7th International Conference on Smart and Sustainable Technologies (SpliTech)*, 2022. https://doi.org/10.23919/splitech55088.2022.9854243.